ACS OMEGA

Open Access

http://pubs.acs.org/journal/acsodf

Article

Quasi-Solid-State Zn-Ion Batteries Based on Sol–Gel Transition and in Situ Electrodeposition of MnO_2

Peng Wang and Petru Andrei*

Cite This: *ACS Omega* 2025, 10, 16589–16596

Read Online

ACCESS | Metrics & More | Article Recommendations | Supporting Information

ABSTRACT: Zinc-ion batteries (ZIBs) have received much attention recently, because they are low-cost and environmentally friendly. In addition, ZIBs can be safer than lithium-ion batteries (LIBs) if issues, such as dendrite formation, side reactions, and hydrogen evolution, are resolved. Overcoming these challenges is crucial for the large-scale commercialization of ZIBs. In this article, Kevlar derivatized Aramid nanofiber combined with poly(vinyl alcohol) hydrogel was used to prevent the Zn dendrite growth and side reactions and increase the cyclability of the cells. A fast and simple method that involves sol–gel transition and in situ electrodeposition of the MnO_2 cathode was developed to fabricate quasi-solid-state ZIB cells with an initial capacity of 5.2 and 3.3 mA h after 900 cycles at 10C. In addition, we have optimized the assembling process of ZIBs pouch cells by taking advantage of sol–gel transition and eliminating the conventional complex slurry-casting-drying steps. This work paves the way to efficiently assemble ZIB pouch cells with excellent rate performance and cycling stability.

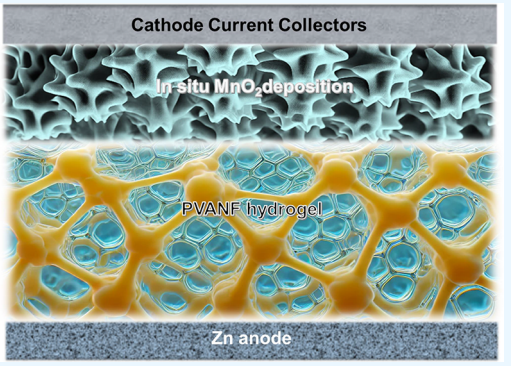

INTRODUCTION

To keep pace with higher-quality demand in modern life, flexible, wearable, and multifunctional electronic devices are now a prominent focus in the digital device market. These smart and flexible electronics put stringent requirements to their power sources, such as batteries and supercapacitors.[1−5] Therefore, it is imperative to develop energy storage devices that combine flexibility, wearability, and dependable electrochemical performance, and be safe at the same time.[6] Among various energy storage devices, aqueous zinc-ion batteries (ZIBs) offer significant potential as power sources for flexible electronics thanks to their high safety, low cost, high theoretical capacity (820 mA h g^{-1}), and proper redox potential (−0.763 V vs Standard Hydrogen Electrode, SHE).[7−11] However, the practical application of ZIBs still encounters many challenges, such as dendrite growth due to uneven Zn deposition at the anode, side reaction because of water splitting reactions, poor cathode stability that limits the cycling life, and liquid leakage.[12−15] To overcome these problems, diverse strategies have been developed, such as Zn anode surface protection, Zn anode structure design, electrolyte additive adjustment, and electrolyte system transformation (for example, hydrogel and solid electrolyte).

Hydrogels can host a significant quantity of aqueous electrolytes, offering high ion conductivity and retaining electrolyte over their long cycle life due to their numerous hydrophilic groups and three-dimensional network structure.[16−19] Effective Zn^{2+} deposition and suppressed Zn dendrite growth could be achieved through interactions with functional groups in 3D network structures, and close contact with hydrogel due to abundant polar groups and mechanical elasticity.[20,21] Recent advancements in the development of hydrogels for ZIBs have evolved from basic designs that primarily emphasize mechanical properties, ionic conductivity, and the suppression of Zn dendrites to more sophisticated systems that address environmental durability, particularly under extreme temperature conditions.[16,22] As the application scope of hydrogel-based ZIBs has expanded, certain limitations have become apparent, such as the freezing of hydrogels at subzero temperatures and electrolyte dehydration at elevated temperatures. Consequently, recent research has shifted its focus toward developing advanced functional hydrogels designed to address these challenges and improve the performance and reliability of ZIBs under a wider range of environmental conditions.[23,16,24−26]

While recent research has been centered on improving the functional properties of hydrogels, our work emphasizes the importance of their fabrication and integration into fully assembled ZIBs. The fabrication of hydrogel based ZIBs is complex and time-consuming, involving cathode (mixing slurry, casting, and drying) and hydrogel (mixing monomers, polymerizing, and adding electrolyte).[27−29] Then, the battery

Received: December 31, 2024
Revised: April 4, 2025
Accepted: April 11, 2025
Published: April 18, 2025

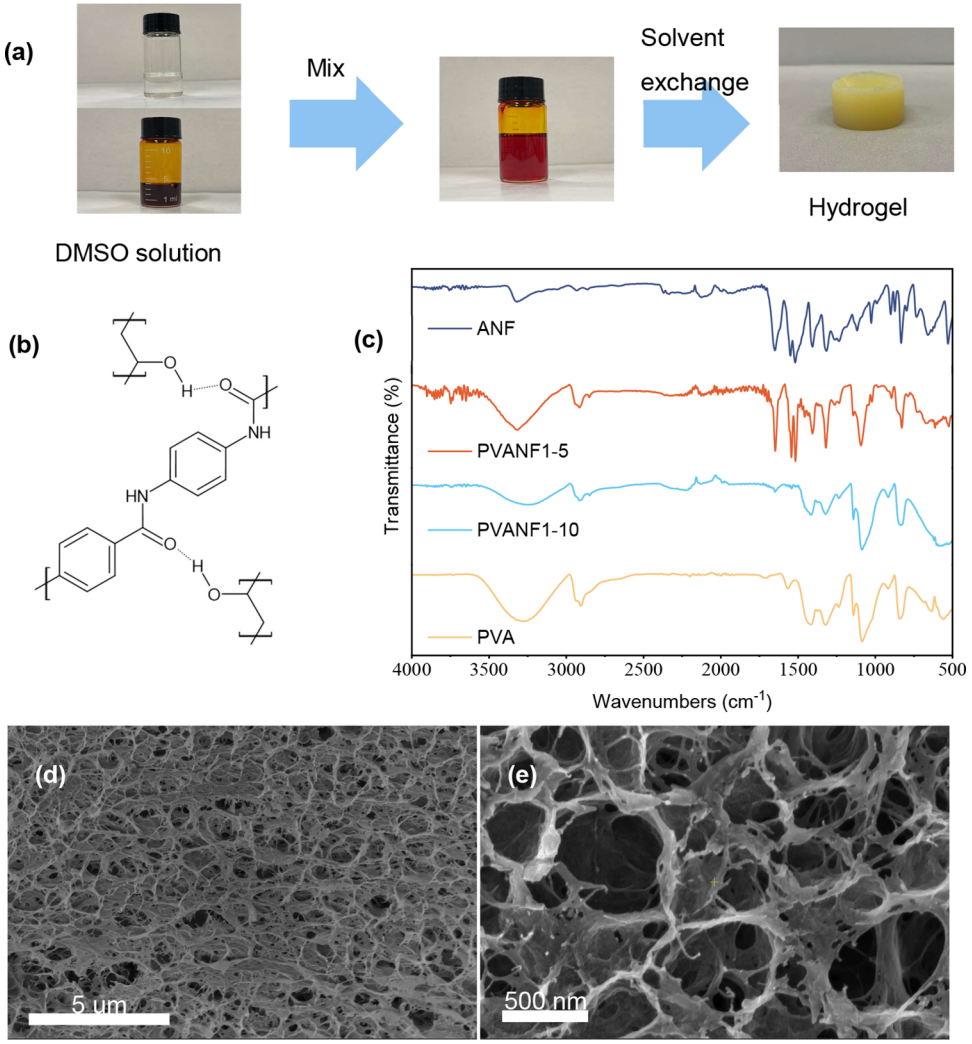

Figure 1. Design principle and structure of the PVANF. (a) Schematic illustration of preparation of PVANF, (b) Hydron bond between PVA and ANF polymer chains, (c) FTIR spectra of PVA, ANF and PVANF. SEM of surface (d) and cross-section (e) of PVANF1−5.

components, including the cathode, anode, and electrolyte, are assembled. In this study, we focus on the design of hydrogels and their integration into full ZIBs. Ingeniously taking advantage of the sol−gel transition process of poly(vinyl alcohol) (PVA) and aramid nanofiber (ANF)-based hydrogel, we explored in situ casting and gelation techniques directly on the cathode current collector, which allows for a more uniform and intimate contact between the hydrogel electrolyte and the electrode materials.[30] Additionally, inspired by previous a publication,[31] the in situ electrodeposition of MnO_2 on the current collector was applied, which not only simplifies the assembly of the battery, especially the cathode fabrication, but also improves the electrochemical performance of the system. The PVA component maintains a hydrated environment, ensuring efficient ion transport and stable ion concentration at the electrode surface, which helps to prevent uneven Zn deposition and dendrite formation. Meanwhile, the ANFs provide a robust network that influences the electric field distribution, promoting uniform Zn deposition. Benefiting from the excellent synergistic effect of the PVA and ANF, the emerging poly(vinyl alcohol) and aramid nanofiber (PVANF) hydrogel electrolyte has demonstrated a high Coulombic efficiency of 99.99% during Zn plating/stripping over 1000 h. In addition, the PVANF hydrogel enables uniform in situ electrodeposition of MnO_2 on the cathode. In full cell configurations, this prototype pouch cell achieves a capacity of 9.5 mA h (1.9 mA h cm^{-2}) along with excellent long-term cycling stability, indicating the advantages of our strategy in battery performance.

EXPERIMENTAL SECTION

Preparation of the PVANF Hydrogel Electrolyte. The preparation of the ANF in dimethyl sulfoxide (DMSO) dispersion was conducted using the method initially developed by Yang et al.[32] and modified by Yang et al.[33] In this process, 2.0 g of Kevlar 49 fibers and 3.0 g of KOH were added to 98.0 g of DMSO. The resulting suspension underwent probe sonication for 1 h into an ice−water bath, followed by mechanical stirring at 500 rpm for 1 week at room temperature. A 10 wt % PVA solution in DMSO was prepared by dissolving 5.0 g of PVA (Sigma-Aldrich, M_w 146,000−186,000 au, 99%+ hydrolyzed) in 45.0 g of DMSO, followed by magnetic stirring at 90 °C and 500 rpm for 5 h. The resulting ANFs/DMSO dispersion (5 wt %) was then mixed with the PVA/DMSO solution in weight ratios of 1:1 and 1:2. After 20 min of mixing, the mixture was cast onto a glass plate using a doctor blade then submerged in 2 M $ZnSO_4$ + 0.2 M

https://doi.org/10.1021/acsomega.4c11717
ACS Omega 2025, 10, 16589−16596

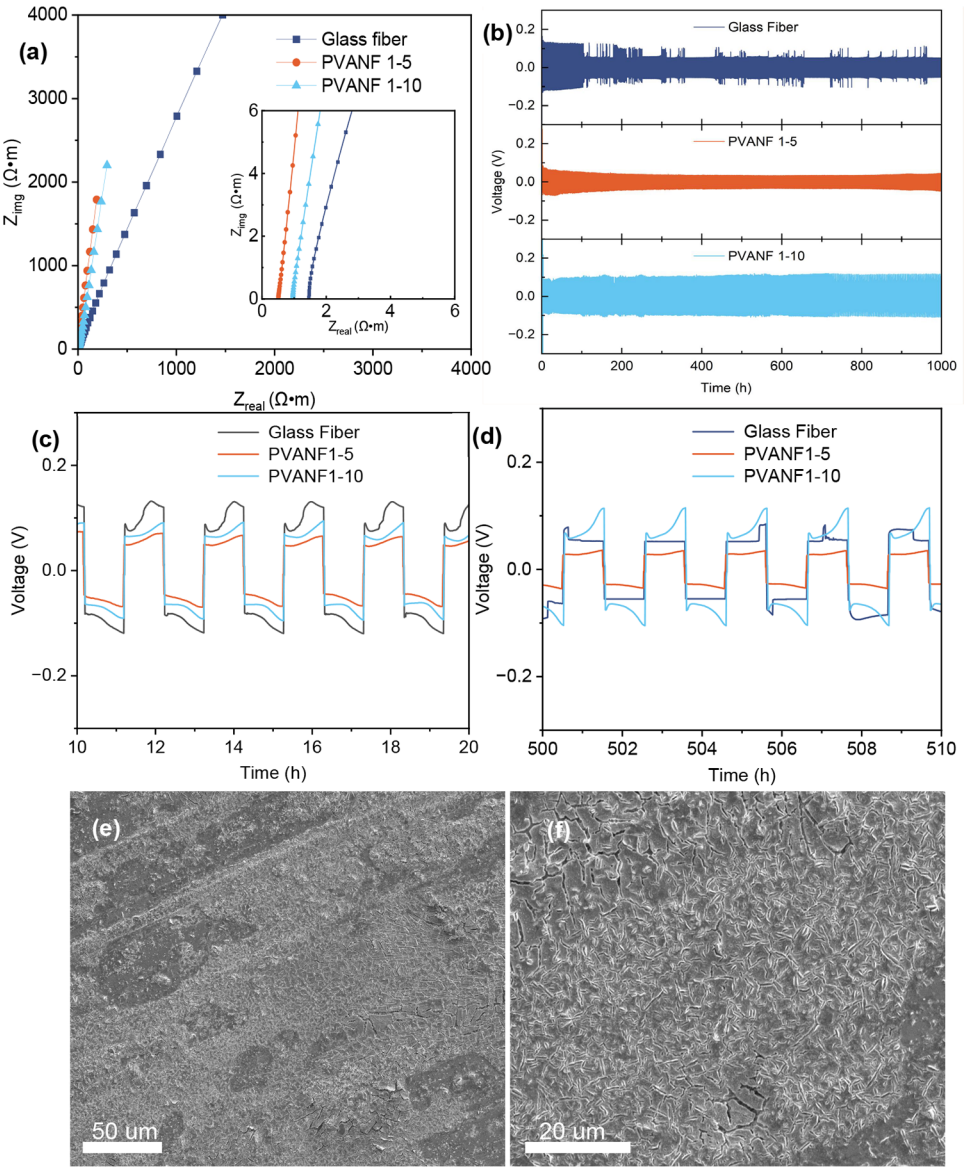

Figure 2. Evaluation of PVANF in Zn symmetric cells. (a) Ionic conductivity measurement (all the hydrogels used for the ionic conductivity test and further electrochemical tests were soaked in 2 M $ZnSO_4$ + 0.2 M $MnSO_4$ solution for 24 h). (b–d) Zn plating/stripping cycling test. (e, f) SEM image of the Zn surface with PVANF1–5 after 500 h cycles.

$MnSO_4$ solution for 24 h, resulting in the formation of the PVANF hydrogel electrolyte.

Simple and Fast Assembly of the ZIB Full Cell. To assemble the ZIBs full cell, the above hydrogel mixture solution was uniformly cast onto the cathode current collector, ensuring consistent coverage. The coated cathode was then immersed in a 2 M $ZnSO_4$ + 0.2 M $MnSO_4$ solution for 24 h to facilitate the appropriate solvent exchange, electrolyte absorption and sol–gel transition of the hydrogel. Following this incubation period, a Zn anode was carefully positioned onto the hydrogel-coated cathode, thus completing the assembly of the electrochemical cell for subsequent experimental analysis.

Characterization. The morphologies of the PVANF hydrogel (after freeze-drying) and in situ electrodeposited MnO_2 on the current collector were observed by Field Emission Scanning Electron Microscopy (FESEM, FEI Helios G4 UC) equipped with mapping images for elemental analysis. The microstructure of the aramid nanofiber was characterized via Transmission Electron Microscopy (TEM, JEM-ARM200cF). The phase and structure of in situ electrodeposited MnO_2 on the current collector were identified by X-ray diffraction (XRD, Rigaku SmartLab) employing Cu Kα radiation from 10° to 80°. Fourier transform infrared spectroscopy (FT-IR spectroscopy, JASCO 6800) was utilized to study the functional groups in the PVANF hydrogel. The mechanical tensile-stress properties of the hydrogels were measured using the tensile stress–strain test conducted by a Dynamic Mechanical Analysis machine (DMA, Rheometer ARES-G2) at a tensile speed of 1 mm min^{-1}. The samples used in the experiments were prepared as dumbbell-shaped materials (30 mm × 2 mm × 0.2 mm).

Electrochemical Measurements. Galvanostatic charge/discharge (GCD) measurements were examined using a Neware battery testing system (Shenzhen, China) to evaluate the cyclic performance. Cyclic voltammetry (CV) testing along with the ionic conductivity measurement was acquired with Gamry Reference 3000 (Warminster, PA, USA). Different scan

https://doi.org/10.1021/acsomega.4c11717
ACS Omega 2025, 10, 16589–16596

rates were employed to test CV curves of batteries, and the voltage was tested from 1 to 1.8 V (vs Zn^{2+}/Zn). The ionic conductivity was recorded by electrochemical impedance spectroscopy (EIS) tests in the range of 1×10^{-1}−10^{6} Hz.

RESULTS AND DISCUSSION

As shown in Figure 1a, the PVANF was obtained by mixing the PVA/DMSO solution and the ANF/DMSO dispersion, and then the DMSO solvent was exchanged during sol−gel transition by submerging in a 2 M $ZnSO_4$ + 0.2 M $MnSO_4$ solution. Mixing the ANF dispersion and a PVA solution leads to a viscous fluid that can be cast on a glass plate or other substrates. Since DMSO is highly soluble in water, it is easily replaced by water due to concentration gradients that appear during immersion in the aqueous $ZnSO_4/MnSO_4$ solution. The color change of the mixed solution from dark red to yellow during sol−gel transition indicates that the DMSO was replaced by the aqueous electrolyte. This exchange promotes hydrogen bonding between PVA and ANF, resulting in gelation. Any DMSO residue left in the PVANF improves the performance of the ZIBs by preventing the Zn dendrite growth.[34,35] The relationship between the residue DMSO amount, electrochemical performance of ZIBs and solvent exchange time is worth exploring in the future. The hydrogels used in this study have an ANF-to-PVA weight ratio of 1:5 and 1:10 with similar liquid content levels (∼94 wt % aqueous electrolyte), denoted as PVANF1−5 and PVANF1−10. In this study, we have focused on ANF:PVA weight ratios of 1:5 and 1:10 to investigate their effects on the hydrogel's mechanical strength and ionic conductivity. This approach allowed us to integrate the sol−gel process directly into the cathode fabrication, streamlining the production and ensuring consistency in our experimental setup. While intermediate ratios were not explored in this work, existing literature suggests that varying the ANF:PVA ratio can influence the hydrogel's properties. For instance, adjusting the polymer composition has been shown to affect the mechanical robustness and conductivity of similar hydrogels.[36,37] Exploring intermediate ratios could potentially optimize the balance between the mechanical and ionic properties.

Fourier transform infrared (FTIR) was employed to provide insight into the interactions between PVA and ANF, as shown in Figure 1c. The sharp peaks at 3316 and 1641 cm^{-1} are attributed to the N−H stretching, amide C=O stretching vibration, while the peaks at 1540 and 1505 cm^{-1} are attributed to C=C stretching vibration within the aromatic ring in the case of ANF. The broad peak ranging from 3000 to 3500 cm^{-1} and the peak at 2900 cm^{-1} are attributed to the O−H stretching and alkanes C−H stretching vibration in the case of PVA. Obviously specific peaks for ANF and PVA appear in PVANF1−5 with a broad but sharp peak at 3317 cm^{-1} because of the overlap of the O−H and N−H stretching vibration. PVANF1−10 shows all intensive peaks for PVA but weak peaks for ANF (1647 cm^{-1} for the C=O stretching vibration), mainly because of the abundant PVA compared to PVANF1−5. A distinct red shift of the aramid C=O stretching band in PVANF composites compared to bare ANF is evidence of hydrogen bonding between the stiff (ANF) and soft (PVA) components, as shown in Figures 1b and S2.

Scanning electron microscopy (SEM) reveals the microscale morphology of PVANF hydrogels, revealing that nanofibers form a uniform, highly interconnected network, as shown in Figure 1d,e. The inherent flexibility and branching of individual ANFs enhance the structural integrity of the hydrogel, as shown in Figure S1.[38] The microscale morphology of PVANF can be affected by the ratio of ANF and PVA. PVANF1−5 demonstrates a uniform, homogeneous, and tidy structure with a pore size below 500 nm, whereas PVANF1−10 shows a random and flake-like structure resulting from an excess of PVA in Figure S3. The microscale structure of the hydrogel affects the connection of the water/solution inside and Zn ion diffusion. PVANF1−5 shows a preferred structure and provides a better Zn ion transfer path when applied for ZIBs. Tensile strength tests were used to understand the effect of the interaction between ANF and PVA. PVANF1−5 showed a tensile strength of 3.8 MPa and Young's modulus of 30 MPa in Figure S4, while the addition of more PVA (PVANF1−10) resulted in a reduction of both properties (1.2 and 2.5 MPa), corresponding to its microscale structure shown in Figure S3. Extensive interfacial interactions between the nanoscale components are responsible for their mechanical property. A uniform and 3D connected microstructure resulting from superior interfacial interactions between the ANF framework and PVA shows improved mechanical properties.

The ionic conductivities of the hydrogels were evaluated by AC impedance, as shown in Figure 2a. Glass fiber (GF, Whatman, thickness of 200 μm) soaked excess electrolyte was employed to assess conductivity and further tests as a comparison. The ionic conductivity of PVANF1−5 showed an excellent value of 19.7 mS cm^{-1}, while glass fiber and PVANF1−10 hydrogels reached 6.9 and 10.4 mS cm^{-1}. The high ionic conductivity for PVANF1−5 stemmed from ordered and uniform pores, which provide abundant accommodation for electrolyte and a better ion transfer path. The symmetrical Zn cells were employed to determine the plating/stripping performance of the PVANF hydrogels. The batteries with both PVANF1−5 and PVANF1−10 in Figure 2b demonstrated stable cycling for more than 1000 h at a current density of 0.5 mA cm^{-2} (0.5 mA h cm^{-2}). On the contrary, symmetrical cells with glass fiber can cycle no more than 100 h because of the formation of short circuits by the uncontrollable dendrite formation and side reactions. Remarkably, the overpotential of PVANF1−5 (0.07 V vs Zn^{2+}/Zn) was lower than that of glass fiber (0.13 V) and PVANF1−10 (0.09 V), and it decreased gradually to 0.035 V after around 500 h. The plating curve for glass fiber has multiple up-and-down variations during the first couple of dozen of cycles (this can be seen in Figure 2c, which shows the cycles from 10 to 20 h), indicating the instability and/or parasitic reactions in the zinc plating and stripping process.[39,40] On the contrary, PVANF1−5 and PVANF1−10 showed only a slowly increasing overpotential, as seen in Figure 2d. After 500 h cycling, PVANF1−5 showed an even flatter and more stable potential plateau, suggesting efficient, uniform zinc deposition and dissolution, stable electrode/electrolyte interface, and limited side reactions.[16,23,24] The superior stability of PVANF1−5 in symmetric cells was confirmed by SEM images of the Zn surface after plating and stripping for 500 h. Compared to large Zn dendrite aggregated with glass fiber in Figure S5a,b, PVANF1−5 in Figure 2e,f and PVANF1−10 in Figure S5c,d showed fine and small Zn grains without dendrites. The PVANF hydrogel regulates Zn deposition in ZIBs through hydration, structural support, and ion management benefited from the combination of ANF and PVA. The PVA component maintains a hydrated environment that enables efficient ion transport and stable concentration at the electrode surface, reducing the risk of

https://doi.org/10.1021/acsomega.4c11717
ACS Omega 2025, 10, 16589−16596

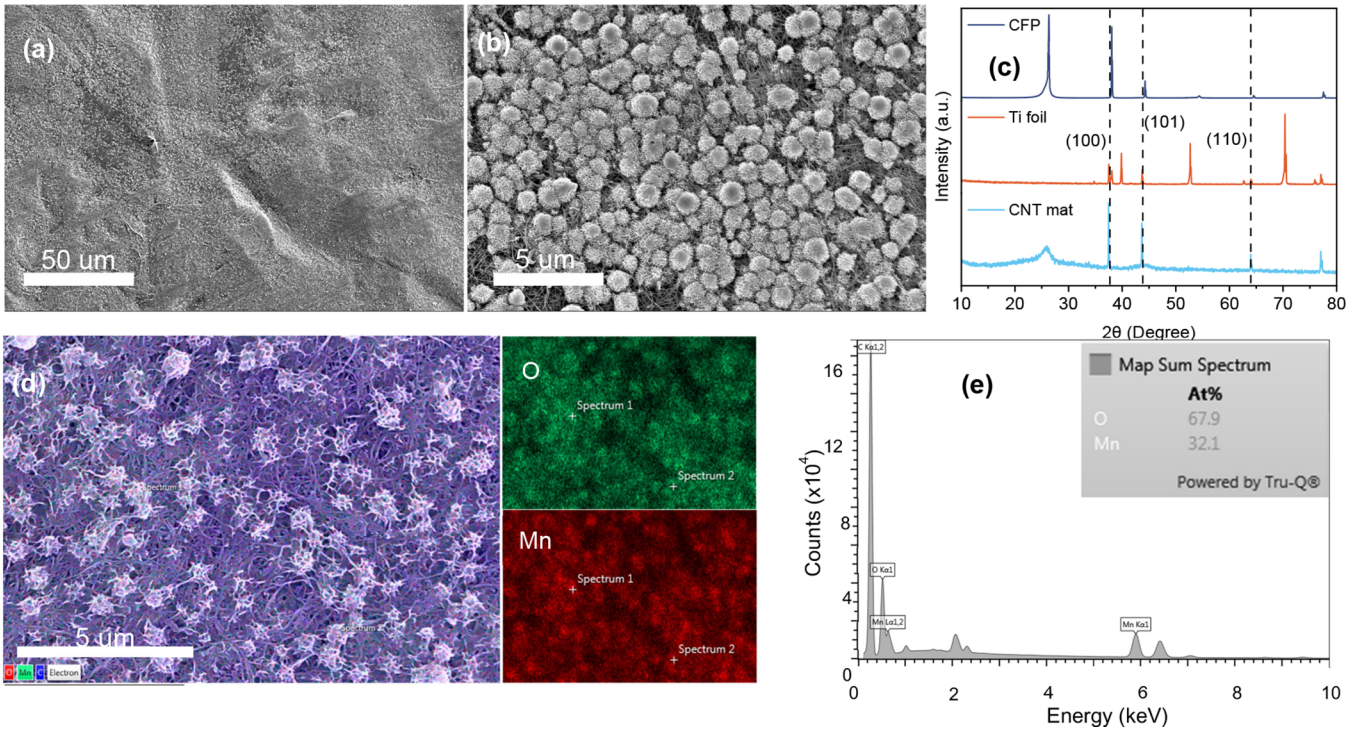

Figure 3. Characterization of in situ electrodeposited MnO_2. (a, b) SEM images of MnO_2 on CNT mat with different magnitudes. (c) XRD pattern of MnO_2 deposited on various current collectors. (d, e) EDS mapping and elements distribution of MnO_2 on CNT mat.

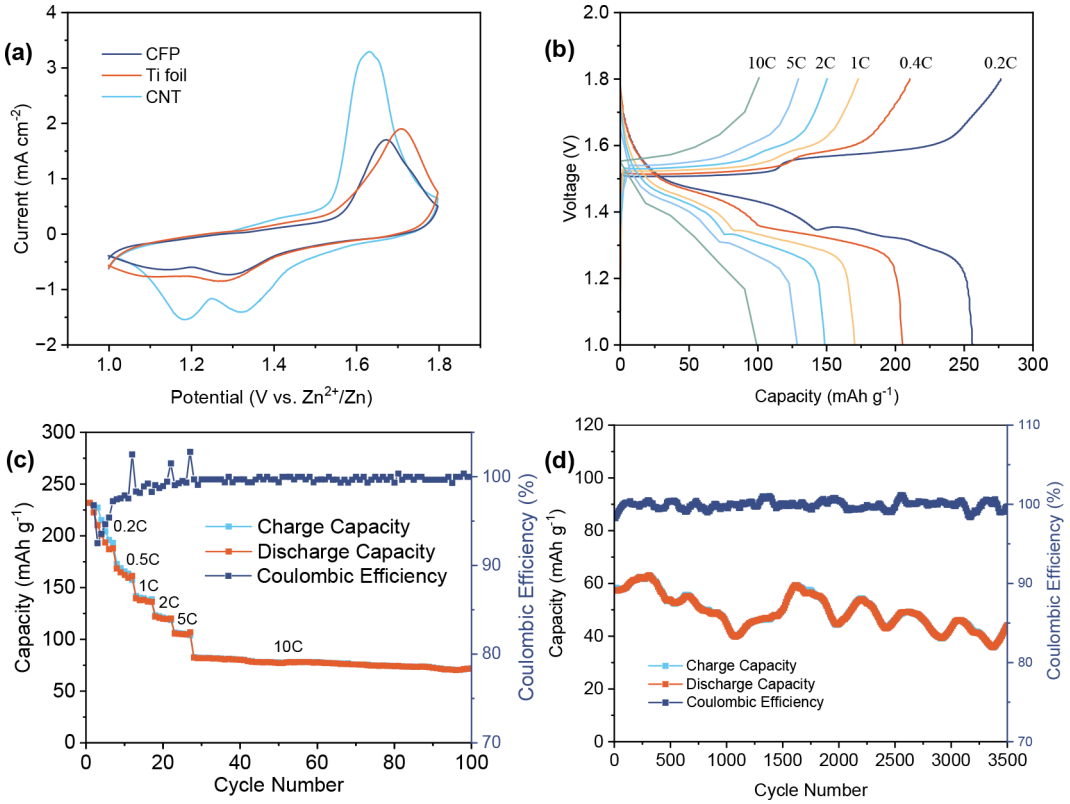

Figure 4. Electrochemical analysis of in situ deposited MnO_2. (a) CV curves of MnO_2 deposited on different substrates. (b–d) Charge/discharge curves, rate (0.2C, 0.5C, 1C, 2C, 5C, and 10C) and cycle performance (10C) of MnO_2 on the CNT mat.

uneven Zn deposition. Meanwhile, the ANFs form a robust network that directs Zn ions to deposit uniformly, minimizing the dendrite formation. Additionally, the polymer matrix in the hydrogel acts as a Zn ion reservoir, preventing concentration spikes, while its elasticity accommodates volume changes, reducing stress on the electrode.

To decrease the assembly time of ZIBs cells, the cathode fabrication needs to be simplified. Inspired by a previous

https://doi.org/10.1021/acsomega.4c11717
ACS Omega 2025, 10, 16589−16596

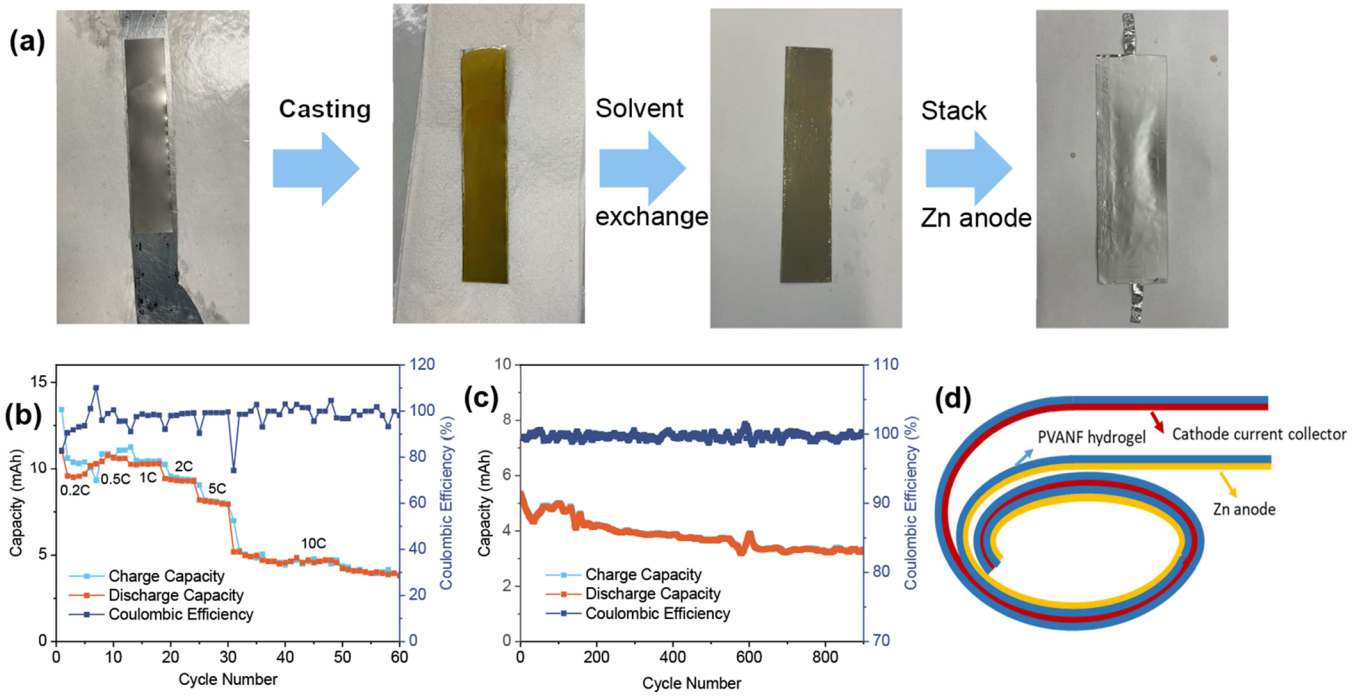

Figure 5. Assembly and electrochemical analysis of ZIB pouch cell. (a) Steps taken during the fabrication of ZIB pouch cells. (b, c) Rate (0.2C, 0.5C, 1C, 2C, 5C, and 10C) and cycling performance (10C) of the ZIB pouch cell. (d) Sketch showing the assembly of cylindrical cells with the PVANF hydrogel.

publication,[31] in situ electrodeposition of MnO_2 on the current collector was used to save conventional steps (mixing slurry, casting and drying). Different current collectors including carbon fiber paper (CFP), Ti foils, and carbon nanotube (CNT) mat were employed for in situ electrodeposition of MnO_2. Given by the best plating/stripping cycling stability and lowest overpotential in symmetric cells, PVANF1−5 was chosen for further application for in situ electrodeposition. To electrodeposit MnO_2 on various current collectors, the precursor solution for PVANF1−5 (solution mixture of ANF/DMSO and PVA/DMSO) was cast on different current collectors and underwent solvent exchange in 2 M $ZnSO_4$ + 0.2 M $MnSO_4$ for 24 h. During the assembly of the coin cells, the coated current collector was used as the cathode and Zn as the anode. The above cells were charged to 1.8 V vs Zn^{2+}/Zn at a constant current density of 0.2 mA cm^{-2} and a then constant voltage of 1.8 V vs Zn/Zn^{2+} for 8 h to electrodeposition of MnO_2, according to the reaction:

$$Mn^{2+} + 2H_2O \rightarrow MnO_2 + 4H^+ + 2e^-$$

The electrodeposition parameters (i.e., current density, deposition time, and $MnSO_4$ concentration) are critical in determining the morphology and properties of MnO_2 coatings. Variations in these parameters can significantly influence the nucleation and growth mechanisms, leading to different morphological features. For instance, by adjustment of the deposition time, the MnO_2 morphology can transition from initial nucleation stages to more developed structures, as observed in studies where prolonged deposition led to changes in surface characteristics. In our study, we have adopted a number of parameters that were already optimized in the literature,[31] specifically charging cells to 1.8 V vs Zn^{2+}/Zn at a constant current density of 0.2 mA cm^{-2}, followed by maintaining a constant voltage of 1.8 V vs Zn/Zn^{2+} for 8 h to achieve uniform MnO_2 electrodeposition.

The SEM images in Figures 3a,b and S6 show that the surface of all three current collectors was conformally covered by MnO_2. The elemental mapping images in Figure 3d,e indicate the uniform distribution of Mn and O, and the atomic ratio of Mn to O is around 1:2. Figure 3c shows the XRD pattern of the obtained MnO_2 electrodes. Major diffraction peaks showed in all three current collectors with 2-theta values around 37.0, 42.5, and 66.9 degrees corresponding to the (100), (101), and (110) planes for Akhtenskite MnO_2 (JCPDS 30-0820). The peak expected at 55° is absent, which may be attributed to low intensity below the detection limit or affected by orientation. Despite this missing peak, the overall pattern, as well as the atomic ratio of Mn to O around 1:2, strongly suggests the presence of Akhtenskite MnO_2.

After electrodeposition, the cells were tested using cyclic voltammetry (CV) and cycled similarly to the Zn/MnO_2 cells. Figure 4a exhibits the CV curves of Zn/MnO_2 cells on different current collectors with a scan rate of 0.1 mA s^{-1} within a potential window from 1 to 1.8 V vs Zn^{2+}/Zn. The CNT-based cell shows two oxidation peaks that overlap around 1.63 and 1.65 V and two well-separated reduction peaks at 1.18 and 1.32 V, corresponding to a two-step reaction.[31] However, the CFP and Ti foil-based cells show one oxidation peak and two reduction peaks, indicating the complete overlap of two oxidation peaks. This is due to the high crystallinity of MnO_2, which limits the diffusion of Zn ions.[31] Given the higher current density at oxidation and reduction peaks in the CV curve, CNT-based cells were employed for galvanostatic charge/discharge cycling. The first cycle charge/discharge curves at different C rate range from 0.2C to 10C are shown in Figure 4b, where both charge and discharge show two distinct plateaus at various C rates, corresponding to two pairs of redox peaks in the CV curve.

https://doi.org/10.1021/acsomega.4c11717
ACS Omega 2025, 10, 16589−16596

The first voltage plateau of the discharge curve is attributed to H^+ insertion, while the second plateau to Zn^{2+} insertion.[31] The cell showed a high capacity of 265 mA h g^{-1} (based on weight of MnO_2) at 0.2C and 100 mA h g^{-1} at 10C for the first cycle. The cell also showed excellent rate performance and a steady capacity of 75 mA h g^{-1} at 10C, as shown in Figure 4c. After 3500 cycles at 10 °C, it still had a large capacity of 50 mA h g^{-1}. The fluctuations of the capacity of the MnO_2 cathode that appear during the cycling at 10C are most likely caused by a combination of electrode/electrolyte interface evolution and Zn plating/stripping behavior over long-term cycling (see Figure 4d).

To illustrate the efficient assembly of quasi-solid-state ZIB pouch cells, a Ti foil is selected as the cathode current collector because it provides better mechanical support and is easy to handle by hand. The procedure includes mixing PVANF precursor solution, casting on Ti foil, sol−gel transition by exchanging solvent, stacking with Zn and sealing with vacuum, as shown in Figure 5a. There are some advantages and characteristics in our prototype cell fabrication: (1) no cathode slurry making, casting, and drying steps; (2) the PVANF hydrogel was cast directly on the current collector; (3) the aqueous electrolyte was soaked in the hydrogel during the sol−gel transition step by solvent exchange; and (4) cells were precharged to in situ electrodeposit MnO_2 on the current collectors to obtain active materials. The as-prepared ZIB pouch cells were assessed for a performance rate range from 0.2C to 10C within 1 to 1.8 V vs Zn^{2+}/Zn and cycling stability at 10C in Figure 5b. The capacity of the pouch cell reached 9.5 mA h (1.9 mA h cm^{-2}) at 0.2C, 8.1 mA h (1.62 mA h cm^{-2}) at 5C and 5.2 mA h (1.04 mA h cm^{-2}) at 10C. High C-rate accelerates Zn plating/stripping, making it an effective way to test the electrode/electrolyte interface stability, resistance to dendrite formation, and overall reversibility. The fluctuations observed at the 10C rate are believed to be primarily due to kinetic limitations and diffusion processes. At these C-rates, the rapid Zn plating/stripping process leads to less uniform deposition and reduced Coulomb efficiency. The cell delivered a stable cycling capacity of 3.3 mA h (0.66 mA h cm^{-2}) at 10C after 900 cycles in Figure 5c, showing the potential of our battery design for high-power applications. Compared to the large Zn dendrites observed in Figure S5a,b, the Zn surface in full cells, as shown in Figure S7a,b, with the PVANF hydrogel exhibits uniform deposition without obvious dendrites, evidencing that our approach effectively suppresses Zn dendrite growth and side reactions.

In this study, we have demonstrated the feasibility of integrating our PVANF hydrogel technology to electrodeposit MnO_2 directly onto cathode current collectors, which is a scalable approach for large-scale battery production, including cylindrical cells, as shown in Figure 5d. However, we acknowledge that the MnO_2 loading achieved in our current setup is not yet sufficient for practical applications. To address this, future research will focus on optimizing the electrodeposition parameters, such as electrolyte concentration and deposition time, to increase the MnO_2 loading. Additionally, exploring alternative fabrication techniques, such as screen-printing, could further enhance scalability and performance. By improving MnO_2 loading and refining our methods, we aim to develop a practical and efficient strategy for large-scale battery production.

CONCLUSIONS

A new method for the fabrication of ZIB full cells including pouch cells is proposed by taking advantage of the sol−gel transition of PVANF and in situ electrodeposition of MnO_2 as cathode active materials. PVANF hydrogel showed a high ionic conductivity of 19.7 mS cm^{-1} and stable plating/stripping for 1000 h due to the improved structure and component design. Complex procedures for cathode fabrication involving slurry mixing, casting, and drying can be avoided by in situ electrodeposition of MnO_2 directly on the current collector. The deposited MnO_2 on the CNT mat showed high capacity of 265 mA h g^{-1} and retained 50 mA h g^{-1} after 3500 cycles at 10C. The only step which took a long time is solvent exchange involved the sol−gel transition and electrolyte "injection" in hydrogel, which could potentially be significantly shortened and achieve better performance simultaneously. Using this strategy, a prototype pouch cell with a high capacity of 9.5 mA h (1.9 mA h cm^{-2}) at 0.2C, 5.2 mA h (1.04 mA h cm^{-2}) at 10C was fabricated. The cell retained 3.3 mA h (0.66 mA h cm^{-2}) after 900 cycles at 10C. Compared to the large Zn dendrites observed in Figure S5a,b, the Zn surface in full cells (Figure S7) with the PVANF hydrogel exhibits uniform deposition without obvious dendrites. This provides direct evidence that our approach effectively suppresses Zn dendrite growth and side reactions. Our proposed strategy can be further developed and optimized for both practical flexible ZIBs and scalable cylindrical ZIB cells.

ASSOCIATED CONTENT

Supporting Information

The Supporting Information is available free of charge at https://pubs.acs.org/doi/10.1021/acsomega.4c11717.

Experimental methods and additional characterization data (material synthesis, TEM, FTIR, SEM, and tensile test XRD results) (PDF)

AUTHOR INFORMATION

Corresponding Author

Petru Andrei − *Department of Electrical and Computer Engineering, Florida State University, Tallahassee, Florida 32310, United States;* orcid.org/0000-0002-9826-8448; Email: pandrei@fsu.edu

Author

Peng Wang − *Department of Electrical and Computer Engineering, Florida State University, Tallahassee, Florida 32310, United States*

Complete contact information is available at: https://pubs.acs.org/10.1021/acsomega.4c11717

Notes

The authors declare no competing financial interest.

REFERENCES

(1) Liang, Y.; Yao, Y. Designing Modern Aqueous Batteries. *Nat. Rev. Mater.* **2023**, *8* (2), 109−122.

(2) Li, C.; Wu, J.; Ma, F.; Chen, Y.; Fu, L.; Zhu, Y.; Zhang, Y.; Wang, P.; Wu, Y.; Huang, W. High-Rate and High-Voltage Aqueous Rechargeable Zinc Ammonium Hybrid Battery from Selective Cation Intercalation Cathode. *ACS Appl. Energy Mater.* **2019**, *2* (10), 6984−6989.

(3) Zheng, X.; Luo, R.; Liu, Z.; Wang, M.; Sajid, M.; Xie, Z.; Sun, J.; Xu, K.; Song, L.; Yuan, Y.; Jiang, T.; Liu, S.; Chen, N.; Chen, W. A

Practical Zinc-Bromine Pouch Cell Enabled by Electrolyte Dynamic Stabilizer. *Mater. Today* **2024**, *80*, 353−364.
(4) Hong, S.; Choi, Z.; Hwang, B.; Matic, A. Research Trends and Future Perspectives on Zn-Ion Batteries Using Ga-Based Liquid Metal Coatings on Zn Anodes. *ACS Energy Lett.* **2024**, *9* (11), 5421−5433.
(5) Ren, K.-F.; Liu, H.; Guo, J.-X.; Sun, X.; Jiang, F.; Guo, C.; Bao, W.; Yu, F.; Kalimuldina, G.; Kong, L.; Cheng, X.-B.; Li, J. Working Principles of High-Entropy Electrolytes in Rechargeable Batteries. *ACS Energy Lett.* **2024**, *9* (6), 2960−2980.
(6) Liu, J.; Wang, J.; Xu, C.; Jiang, H.; Li, C.; Zhang, L.; Lin, J.; Shen, Z. X. Advanced Energy Storage Devices: Basic Principles, Analytical Methods, and Rational Materials Design. *Adv. Sci.* **2018**, *5* (1), No. 1700322.
(7) Jia, X.; Liu, C.; Neale, Z. G.; Yang, J.; Cao, G. Active Materials for Aqueous Zinc Ion Batteries: Synthesis, Crystal Structure, Morphology, and Electrochemistry. *Chem. Rev.* **2020**, *120* (15), 7795−7866.
(8) Li, C.; Jin, S.; Archer, L. A.; Nazar, L. F. Toward Practical Aqueous Zinc-Ion Batteries for Electrochemical Energy Storage. *Joule* **2022**, *6* (8), 1733−1738.
(9) Zhang, N.; Chen, X.; Yu, M.; Niu, Z.; Cheng, F.; Chen, J. Materials Chemistry for Rechargeable Zinc-Ion Batteries. *Chem. Soc. Rev.* **2020**, *49* (13), 4203−4219.
(10) Li, Y.; Wang, Z.; Cai, Y.; Pam, M. E.; Yang, Y.; Zhang, D.; Wang, Y.; Huang, S. Designing Advanced Aqueous Zinc-Ion Batteries: Principles, Strategies, and Perspectives. *ENERGY Environ. Mater.* **2022**, *5* (3), 823−851.
(11) Kumari, P.; Kundu, R. Zinc-Ion Batteries: Promise and Challenges for Exploring the Post-Lithium Battery Materials. *ACS Appl. Energy Mater.* **2024**, *7* (21), 9634−9669.
(12) Blanc, L. E.; Kundu, D.; Nazar, L. F. Scientific Challenges for the Implementation of Zn-Ion Batteries. *Joule* **2020**, *4* (4), 771−799.
(13) Tang, B.; Shan, L.; Liang, S.; Zhou, J. Issues and Opportunities Facing Aqueous Zinc-Ion Batteries. *Energy Environ. Sci.* **2019**, *12* (11), 3288−3304.
(14) Li, L.; Zheng, Y.; Xu, J.; Peng, B.; Zhu, G.; Wu, J.; Ma, L.; Jin, Z. Structural and Interfacial Engineering Strategies for Constructing Dendrite-Free Zinc Metal Anodes. *ACS Energy Lett.* **2024**, *9* (7), 3269−3289.
(15) Wu, Z.; Chen, X.; Pan, X.; Li, X.; Yao, J.; Jiang, B.; Lv, L.; Wang, H.; Zhang, B.; Wan, H. Advance in Electrolyte for Stable Zinc Anodes in Mild Aqueous Batteries. *ACS Appl. Energy Mater.* **2024**, *7* (3), 834−844.
(16) Ma, R.; Xu, Z.; Wang, X. Polymer Hydrogel Electrolytes for Flexible and Multifunctional Zinc-Ion Batteries and Capacitors. *ENERGY Environ. Mater.* **2023**, *6* (5), No. e12464.
(17) Li, X.; Wang, D.; Ran, F. Key Approaches and Challenges in Fabricating Advanced Flexible Zinc-Ion Batteries with Functional Hydrogel Electrolytes. *Energy Storage Mater.* **2023**, *56*, 351−393.
(18) Xie, X.; Wang, C.; Xie, J.; Dong, H.; Jiao, J.; Sui, G. Construction of Double-Network Hydrogel Electrolytes for Long-Cycle Dendrite-Free Zinc Anodes. *ACS Appl. Energy Mater.* **2024**, *7* (3), 1162−1171.
(19) Liu, Q.; Ji, Z.; Mo, F.; Ling, W.; Wang, J.; Lei, H.; Cui, M.; Zhang, Z.; Liu, Y.; Cheng, L.; Li, W.; Huang, Y. Stable Thermochromic Hydrogel for a Flexible and Wearable Zinc-Ion Yarn Battery with High-Temperature Warning Function. *ACS Appl. Energy Mater.* **2022**, *5* (10), 12448−12455.
(20) Wang, P.; Andrei, P. (Battery Student Slam 8 Award Winner) A Simple and Fast Method to Assemble Flexible and Stable Quasi-Solid-State Zn Ion Pouch Cell. *ECS Meet. Abstr.* **2024**, *MA2024−01* (5), 760.
(21) Li, X.; Wang, H.; Sun, X.; Li, J.; Liu, Y.-N. Flexible Wide-Temperature Zinc-Ion Battery Enabled by an Ethylene Glycol-Based Organohydrogel Electrolyte. *ACS Appl. Energy Mater.* **2021**, *4* (11), 12718−12727.
(22) Qu, K.; Lu, X.; Jiang, N.; Wang, J.; Tao, Z.; He, G.; Yang, Q.; Qiu, J. Eutectic Electrolytes Convoying Low-Temperature Metal-Ion Batteries. *ACS Energy Lett.* **2024**, *9* (3), 1192−1209.
(23) Wang, Y.; Li, Q.; Hong, H.; Yang, S.; Zhang, R.; Wang, X.; Jin, X.; Xiong, B.; Bai, S.; Zhi, C. Lean-Water Hydrogel Electrolyte for Zinc Ion Batteries. *Nat. Commun.* **2023**, *14* (1), 3890.
(24) Yan, Y.; Duan, S.; Liu, B.; Wu, S.; Alsaid, Y.; Yao, B.; Nandi, S.; Du, Y.; Wang, T.; Li, Y.; He, X. Tough Hydrogel Electrolytes for Anti-Freezing Zinc-Ion Batteries. *Adv. Mater.* **2023**, *35* (18), No. 2211673.
(25) Shi, Y.; Wang, R.; Bi, S.; Yang, M.; Liu, L.; Niu, Z. An Anti-Freezing Hydrogel Electrolyte for Flexible Zinc-Ion Batteries Operating at−70 °C. *Adv. Funct. Mater.* **2023**, *33* (24), 2214546.
(26) Yang, P.; Feng, C.; Liu, Y.; Cheng, T.; Yang, X.; Liu, H.; Liu, K.; Fan, H. J. Thermal Self-Protection of Zinc-Ion Batteries Enabled by Smart Hygroscopic Hydrogel Electrolytes. *Adv. Energy Mater.* **2020**, *10* (48), No. 2002898.
(27) Yu, F.; Wang, Y.; Liu, Y.; Hui, H.-Y.; Wang, F.-X.; Li, J.-F.; Wang, Q. An Aqueous Rechargeable Zinc-Ion Battery on Basis of an Organic Pigment. *Rare Met.* **2022**, *41* (7), 2230−2236.
(28) Li, J.; Huang, L.; Lv, H.; Wang, J.; Wang, G.; Chen, L.; Liu, Y.; Guo, W.; Yu, F.; Gu, T. Novel Organic Cathode with Conjugated N-Heteroaromatic Structures for High-Performance Aqueous Zinc-Ion Batteries. *ACS Appl. Mater. Interfaces* **2022**, *14* (34), 38844−38853.
(29) Yao, M.; Yuan, Z.; Li, S.; He, T.; Wang, R.; Yuan, M.; Niu, Z. Scalable Assembly of Flexible Ultrathin All-in-One Zinc-Ion Batteries with Highly Stretchable, Editable, and Customizable Functions. *Adv. Mater.* **2021**, *33* (10), No. 2008140.
(30) Xu, L.; Zhao, X.; Xu, C.; Kotov, N. A. Water-Rich Biomimetic Composites with Abiotic Self-Organizing Nanofiber Network. *Adv. Mater.* **2018**, *30* (1), No. 1703343.
(31) Sun, W.; Wang, F.; Hou, S.; Yang, C.; Fan, X.; Ma, Z.; Gao, T.; Han, F.; Hu, R.; Zhu, M.; Wang, C. Zn/MnO2 Battery Chemistry With H+ and Zn2+ Coinsertion. *J. Am. Chem. Soc.* **2017**, *139* (29), 9775−9778.
(32) Yang, M.; Cao, K.; Sui, L.; Qi, Y.; Zhu, J.; Waas, A.; Arruda, E. M.; Kieffer, J.; Thouless, M. D.; Kotov, N. A. Dispersions of Aramid Nanofibers: A New Nanoscale Building Block. *ACS Nano* **2011**, *5* (9), 6945−6954.
(33) Yang, B.; Wang, L.; Zhang, M.; Luo, J.; Ding, X. Timesaving, High-Efficiency Approaches To Fabricate Aramid Nanofibers. *ACS Nano* **2019**, *13* (7), 7886−7897.
(34) Nian, Q.; Wang, J.; Liu, S.; Sun, T.; Zheng, S.; Zhang, Y.; Tao, Z.; Chen, J. Aqueous Batteries Operated at−50 °C. *Angew. Chem., Int. Ed.* **2019**, *58* (47), 16994−16999.
(35) Feng, D.; Cao, F.; Hou, L.; Li, T.; Jiao, Y.; Wu, P. Immunizing Aqueous Zn Batteries against Dendrite Formation and Side Reactions at Various Temperatures via Electrolyte Additives. *Small* **2021**, *17* (42), No. 2103195.
(36) Wu, W.; Shi, L.; Qian, K.; Zhou, J.; Zhao, T.; Thaiboonrod, S.; Miao, M.; Feng, X. Synergistic Strengthening of PVA Ionic Conductive Hydrogels Using Aramid Nanofibers and Tannic Acid for Mechanically Robust, Antifreezing, Water-Retaining and Antibacterial Flexible Sensors. *J. Colloid Interface Sci.* **2024**, *654*, 1260−1271.
(37) Zhou, Q.; Lyu, J.; Wang, G.; Robertson, M.; Qiang, Z.; Sun, B.; Ye, C.; Zhu, M. Mechanically Strong and Multifunctional Hybrid Hydrogels with Ultrahigh Electrical Conductivity. *Adv. Funct. Mater.* **2021**, *31* (40), No. 2104536.
(38) Yang, B.; Wang, L.; Zhang, M.; Luo, J.; Lu, Z.; Ding, X. Fabrication, Applications, and Prospects of Aramid Nanofiber. *Adv. Funct. Mater.* **2020**, *30* (22), No. 2000186.
(39) Wang, S.; Huang, Z.; Zhu, J.; Wang, Y.; Li, D.; Wei, Z.; Hong, H.; Zhang, D.; Xiong, Q.; Li, S.; Chen, Z.; Li, N.; Zhi, C. Quantifying Asymmetric Zinc Deposition: A Guide Factor for Designing Durable Zinc Anodes. *Adv. Mater.* **2024**, *36* (33), No. 2406451.
(40) Li, Q.; Chen, A.; Wang, D.; Pei, Z.; Zhi, C. "Soft Shorts" Hidden in Zinc Metal Anode Research. *Joule* **2022**, *6* (2), 273−279.

https://doi.org/10.1021/acsomega.4c11717
ACS Omega 2025, 10, 16589−16596